Journal Pre-proofs

Supporting the Photocatalysts on ZrO_2: An Effective Way to Enhance the Photocatalytic Activity of $SrSnO_3$

Luzia Maria Castro Honorio, André Luiz Menezes de Oliveira, Edson Cavalcanti da Silva Filho, Josy Anteveli Osajima, Amer Hakki, Donald E. Macphee, Iêda Maria Garcia dos Santos

Please cite this article as: L.M.C. Honorio, A.L.M. de Oliveira, E.C. da Silva Filho, J.A. Osajima, A. Hakki, D.E. Macphee, I.M.G. dos Santos, Supporting the Photocatalysts on ZrO_2: An Effective Way to Enhance the Photocatalytic Activity of $SrSnO_3$, *Applied Surface Science* (2020), doi: https://doi.org/10.1016/j.apsusc.2020.146991

Supporting the Photocatalysts on ZrO₂: An Effective Way to Enhance the Photocatalytic Activity of SrSnO₃

Luzia Maria Castro Honorio[a, b], André Luiz Menezes de Oliveira[a], Edson Cavalcanti da Silva Filho[b], Josy Anteveli Osajima[b], Amer Hakki[c], Donald E. Macphee[c], Iêda Maria Garcia dos Santos.[a,c*]

[a]*NPE/LACOM - Núcleo de Pesquisa e Extensão/Laboratório de Combustíveis e Materiais, Universidade Federal da Paraíba, João Pessoa –PB 58051-900, Brazil.*

[b]*LIMAV - Laboratório Interdisciplinar de Materiais Avançados, Universidade Federal do Piauí, Teresina –PI, 64049-550, Brazil.*

[c]*Department of Chemistry, University of Aberdeen, Meston Building, Meston Walk, Aberdeen, AB24 3UE, UK.*

Corresponding author. Universidade Federal da Paraíba, CCEN, DQ - Campus 1. Cidade universitária. João Pessoa – PB. 58051-900, Brazil. E-mail: ieda@quimica.ufpb.br

Abstract

Photocatalysts based on SrSnO₃ and SrSnO₃@ZrO₂ were prepared by the modified-Pechini method and applied in the photocatalytic degradation of a textile azo-dye under UV radiation. The photohydroxylation of terephthalic acid and scavengers were employed in order to evaluate the participation of each active species, such as hydroxyl radical, and photogenerated electrons and holes on the photocatalytic process. The band gap structure was evaluated using the Mott Schottky method in combination with UV-visible spectrophotometry. Both samples had high photocatalytic activity, although SrSnO₃@ZrO₂ showed the best decolorization performance ranging from 32% to 98%. This behavior was assigned to the best dispersion of the active phase on the support and to the Sn(II) reduced states, observed by XPS. The participation of hydroxyl radicals in the reaction was confirmed when terephthalic acid was used as probe and by using isopropanol as hydroxyl radical scavenger, which resulted in the inhibition of the photocatalytic process.

Keywords: Perovskite; SrSnO₃; band gap structure; photocatalysis; active species.

Graphical Abstract
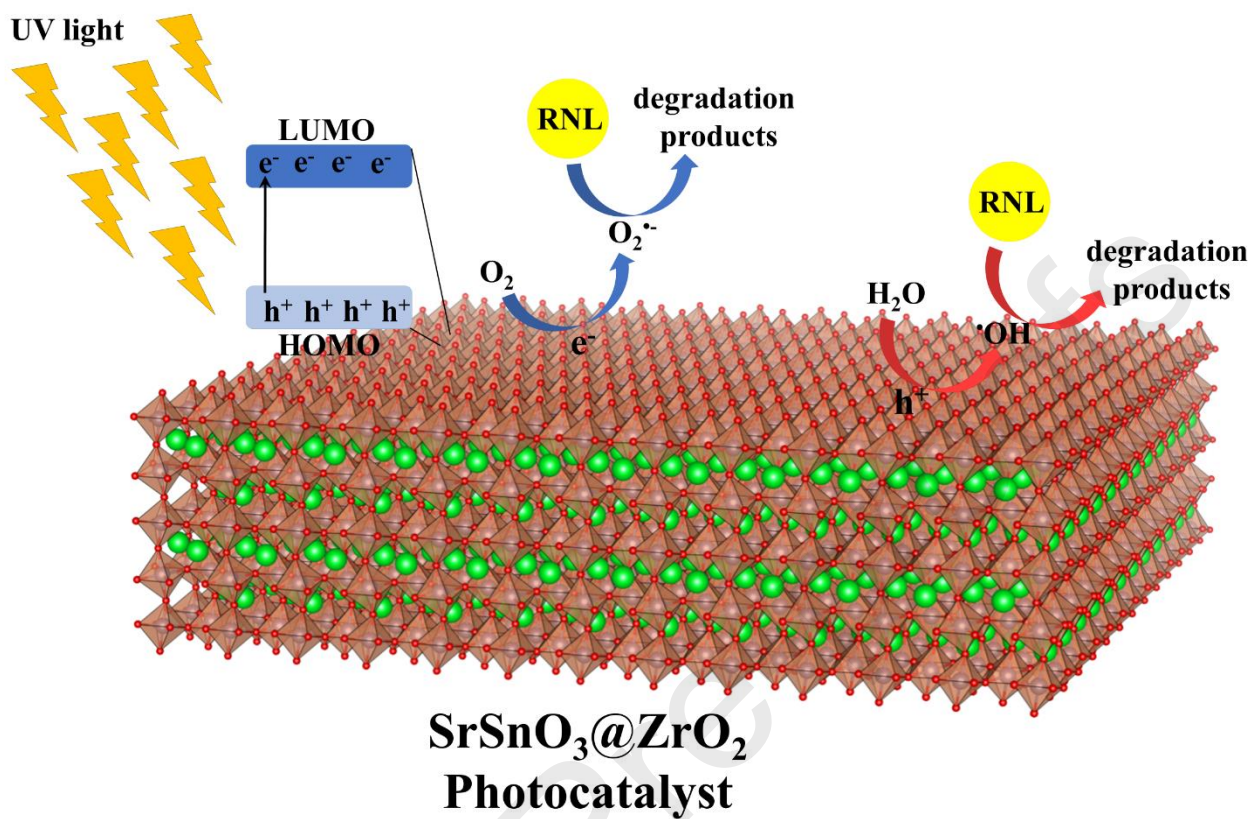
1. Introduction

In recent years the use of synthetic dyes has increased considerably, being extensively used by several industries, such as paper, cosmetics, paints and especially textiles [1,2]. Among the various types of dyes employed in the industries, the azo type, characterized by the presence of the group -N = N- bonded to aromatic groups, constitute more than 70% of the total production, being the most used in the textile industry [2–5]. Because of the complex structure and chemical stability, azo dyes are highly resistant to chemical, photochemical processes and biological treatments, most of which are ineffective for this purpose [5, 6]. Alternative processes for pollutant removal treatment are available, highlighting heterogeneous photocatalysis, an efficient technology for environmental remediation [1, 3].

Recently, alkaline earth stannates ($MSnO_3$, M = Ca^{2+}, Sr^{2+}, Ba^{2+}) have attracted special attention for their promising properties as Li-ion batteries material [7], high temperature humidity sensing [8], solar cells electrodes [9], photoluminescent [10] and photocatalytic [11–15] materials. $SrSnO_3$ is a perovskite with band gap between 2.9 and 4.2 eV [16–18]. It has a distorted orthorhombic-type structure with *Pbnm* space group [19,20] due to the tilting among SnO_6 octahedra [12,20], these distortions playing an important role in the migration of photogenerated charge carriers in $SrSnO_3$, and contributing to its photocatalytic efficiency [12,21]. The use of these perovskites for the photodecomposition of H_2O for H_2 and O_2 generation is also well reported [13,14,22] but few works are reported on its use in textile dye degradation and the reaction pathways [15,23,24]. For instance, Wang *et al*. [25] have applied $CaSnO_3$ microcubes for Methyl orange and Rhodamine B degradation. The degradation percentages were 97 and 99%, respectively, with only 60 min of irradiation, thus indicating that $CaSnO_3$ is a highly efficient material, because of the octahedral tilting in its crystalline network. Moshtaghi *et al*. [26] have prepared $BaSnO_3$ nanostructures and evaluated their photocatalytic efficiency for degradation of an anionic dye, Eriochrome black T. About 84% of degradation was achieved after 120 min under UV light irradiation. Junploy *et al.* [24] have

investigated the photodegradation of methylene blue employing $SrSnO_3$ and obtained 85% of discoloration after 320 min of UV light irradiation. As described by Wang *et al.* [12] and Moshtaghi *et al.* [23] $SrSnO_3$ is considered a promising candidate in the degradation of different dyes. Recently, our research group reported the use of $SrSnO_3$ for the photocatalytic discolorization of the Remazol Golden Yellow dye, giving some insights on charge transfer processes, based on theoretical data, and possible species involved on the photocatalytic process.

It has been established that the photocatalytic activity of the materials depends on their structure and physical properties, such as defects, band gap, surface area and crystallinity, as well as on incorporation of other cations and the use of catalytic supports [3], which can increase surface area, stability and active sites, as a consequence of the strong metal-support interaction.

In view of what was mentioned above, we aimed to prepare two different catalyst forms, the isolated $SrSnO_3$ perovskite and $SrSnO_3$ supported on ZrO_2 ($SrSnO_3@ZrO_2$), to evaluate the influence of this modification on the photocatalytic efficiency of the materials towards Remazol Golden Yellow (RNL) dye photo-degradation. Moreover, we correlated the photocatalytic activity of the materials with their band structure obtained from electrochemical impedance spectroscopy (EIS).

2. Experimental

2.1. Materials

The chemical reagents used in the synthesis of the stannate perovskites were: Metallic tin (Sn, *Vetec* - 99.0%), strontium nitrate ($Sr(NO_3)_2$, *Vetec* - 99.0%), monohydrated citric acid - CA ($C_6H_8O_7.H_2O$, *Cargill* - 99.5%), ammonium hydroxide (NH_4OH, *Vetec* - 99%), ethylene glycol ($C_2H_6O_2$, *Vetec* - 99.5%) and zirconium oxide (ZrO_2, *Aldrich* - 99.0%). For the catalytic tests, the following reagents were used: terephthalic acid ($C_6H_4(COOH)_2$, *Alfa Aesar,* 98+%) isopropyl alcohol ($CH_3CHOHCH_3$, *Moderna* - 99.5%), silver nitrate ($AgNO_3$, *Cennabras* - 99.8%), ethylenediamine

4

tetraacetic acid - EDTA ($C_{10}H_{14}N_2O_8Na_2.2H_2O$, *Vetec* - 99%) and the dye Remazol Golden Yellow - RNL ($C_{16}H_{16}N_4O_{10}S_3.Na_2$ - 566 g mol^{-1}), which was obtained from Dystar.

2.2. Synthesis of the photocatalysts

SrSnO$_3$ powder was synthesized by the *modified-Pechini* method, employing the procedure previously reported by Lucena *et al*. [27]. The formation of the SrSnO$_3$@ZrO$_2$ system was done by the addition of ZrO$_2$ into the polymeric solution in order to obtain 10 mass % of SrSnO$_3$ on the support, followed by the evaporation of solvent using a typical rotary evaporator. The resulting powder was heated at 573 K for 7 h in an oxidant atmosphere, followed by deagglomeration in a mortar and sieving (100 mesh). All the samples were calcined at 1073 K for 4 h, in air at a heating rate of 10 K.min^{-1} to crystallize the desired perovskite phase.

2.3. Characterization

The determination of the amount of SrSnO$_3$ deposited on ZrO$_2$ support was done by X-ray fluorescence (XRF) using a XRF-1800/Shimadzu spectrometer. The materials were then characterized by X-ray powder diffraction (XRD), employing a XRD-6000 Shimadzu diffractometer with CuK$_\alpha$ radiation (λ = 0.15406 Å), scanned between 10-80°, using a step size of 0.02° and step time of 2 s at room temperature. The infrared spectra were obtained with a IRPrestige-21 Shimadzu spectrophotometer, by analysis of a pellet with a 1:100 mass ratio of catalyst:potassium bromide (KBr) on the transmittance mode with a spectral range between 400 and 4000 cm^{-1}. In order to obtain the Raman spectra, a Confocal–WITec spectrophotometer was used, model Alpha 300 S System, coupled to a microscope with an Ar laser (533 nm), 50 mW power, and a Raman shift range between 40 and 1200 cm^{-1} at 25°C. UV-visible spectra were obtained using a UV-2550 Shimadzu spectrophotometer, with a spectral range of 190-900 nm on the diffuse reflectance mode. Tauc's

method [28] was employed to graphically determine the optical band gap energy (E_g) from the UV-vis absorbances of the samples. Microscopy images were obtained by a field emission scanning electron microscope (FE-SEM) from FEI, model FEG250, coupled to an EDS analysis system from Ametek, model HX-1001 with an Apollo X-SDD detector. Samples were dispersed in isopropanol, sonicated for 5 min, dripped on the stub covered with aluminum foil and dried for 2 h. EDX analysis were obtained using a voltage of 25 kV and spot size of 5.5 μm. Transmission electron microscopy (TEM) was performed with a TECNAI LaB$_6$ microscope, under 200 keV voltage. Samples were dispersed in ethanol and deposited on 400 mesh copper grids covered with an ultrathin carbon film of 2-3 nm. X-ray photoelectron spectroscopy (XPS) measurements were carried out with a Scienta Omicron ESCA + spectrometer, system using an Al K$_\alpha$X-ray source with an energy beam of hυ = 1486.87 eV. The binding energies (BE) of the spectra were calibrated relative to C 1s peak position reference centered at 284.6 eV. Surface area determination was carried out using a BEL JAPAN equipment, model BELSORP II-MINI, and zeta potentials were measured at different pH using a Malvern Zetasizer (DSL) Nano ZS system to determine PZC. Evaluation of the conduction band edge was performed using electrochemical impedance spectroscopy (EIS), using the same procedure described by Folli *et al.* [29], except that samples were deposited on ITO glass slides. The spectra were fitted to a Randles circuit to calculate the values for the space charge layer capacitance (C_{sc}), and the details are presented in the Supplementary data.

2.4. *Photocatalytic activity measurement and scavenger experiments*

Photohydroxylation of terephthalic acid - TA was used as a probe to evaluate the formation of hydroxyl radicals by SrSnO$_3$. This reaction produces 2-hydroxyterephthalic acid, a fluorescent substance [22,30,31]. The photocatalytic test was performed according to the procedure described by Teixeira *et al.* [32]. The emission spectra were analyzed in a Hitachi F 2500 fluorescence

spectrophotometer, with excitation wavelength at $\lambda = 320$ nm and monitoring at $\lambda = 426$ nm, which corresponds to the main fluorescence band of the 2-hydroxyterephthalic acid.

The photodegradation tests were performed inside a radiation chamber using 3 UVC OSRAM 9W Puritec HNS S lamps (main emission at $\lambda = 254$ nm). 90 mL of the Remazol RNL dye aqueous solution (10 mg$\square$L^{-1}) and 60 mg of the catalyst were placed in a quartz vessel under magnetic stirring, in order to evaluate decolorization of the dye solution, at pH 3.5 and 6. The samples were placed in the dark for 30 min before the photocatalysis tests, to achieve adsorption/desorption equilibrium. Aliquots of 2 mL of suspension were withdrawn after 1, 2, 4, 6, 8 and 10 h, and centrifuged for 10 min at 5000 rpm, for catalyst separation. The solutions were analyzed by UV-Vis spectroscopy using a SHIMADZU UV-2550 spectrometer, in the range of 300 to 700 nm. The photodegradation reaction of the dye was monitored by measuring the absorbance at $\lambda = 411$ nm (Remazol maximum absorption wavelength), to calculate the percentages of discoloration [33]. Adsorption and photocatalytic tests with scavengers were performed using the same conditions described above.

For the scavenger experiments, isopropyl alcohol (1.6 x 10^{-1} mol L^{-1}) was used as hydroxyl radical inhibitor, silver nitrate (5.0 x 10^{-4} mol L^{-1}) was used to capture photogenerated electrons and EDTA (2.0x 10^{-4} mol L^{-1}) to react with photogenerated holes [32,34,35]. Preliminary tests were carried out in order to determine the optimal amount of the scavengers used in the photocatalytic tests.

3. Results and Discussion

3.1. Characterization of the materials

The XRD patterns of the materials synthesized in the present work are presented in Figure 1. SrSnO$_3$ obtained directly from calcinations of the polymeric resin presented a high crystallinity with well-defined peaks related to orthorhombic structure, space group *Pbnm*-JCPDS n°. 77-1798 (ICSD 188140) [19,36]. SrCO$_3$ was obtained as secondary phase, which has also been noticed by other

7

authors employing different synthesis routes [37,38]. Concerning the system $SrSnO_3@ZrO_2$, it was not possible to identify peaks assigned to the crystalline phase of orthorhombic $SrSnO_3$, which might be due to the amount, or degree of crystallinity, of $SrSnO_3$ deposited on the support. It is important to observe that the diffraction peak at $2\theta = 31.3°$, attributed to (200), (020) and (112) reflections of the $SrSnO_3$ phase, overlap with the diffraction peaks of the ZrO_2 support (monoclinic-type structure, space group $P2_1/c$– ICSD291120) making it difficult to identify $SrSnO_3$ by the conventional XRD technique. Furthermore, no phase transition of the ZrO_2 phase was noticed. The samples were also characterized by Raman spectroscopy and infrared spectroscopy, as shown in the Supplementary data. The responses typically expected for $SrSnO_3$ are absent which, as with the XRD data, may again be indicative of a low degree of crystallinity when deposited on the support.

Figure 1

In order to evaluate the $SrSnO_3@ZrO_2$ formation, this system was analyzed by STEM and TEM techniques, as presented in Figure 2. STEM micrograph (Figure 2a) shows a homogeneous morphology, while the TEM micrograph (Figure 2b) clearly showed the presence of another phase on the catalyst support. The surface phase, $SrSnO_3$, seems to a have a gel-like morphology with a low crystallinity, explaining the XRD and the Raman data, especially when a high crystallinity support is present; XRF results (not shown here), confirmed the presence of $SrSnO_3$ in the $SrSnO_3@ZrO_2$ system, with a final composition of 7:93 mass ratio ($SrSnO_3$:ZrO_2). To confirm the deposition of the active phase on the ZrO_2, elemental mapping was carried out using the STEM/EDX analysis, as displayed in Figure 2c. According to the images, $SrSnO_3$ phase covers the whole sample, as evidenced by the elements that compose the perovskite phase (Sr and Sn) overlapped with that of the support (Zr). This behavior indicates a heterogeneous nucleation process from the polymeric precursor, which leads to a core-shell-like structure [39].

Figure 2

Specific surface area measurements were also performed. The surface area obtained for the SrSnO$_3$ calcined at 800 °C was 20.6 m^2 g^{-1}, corresponding to a particle size of 47.5 nm. Comparison with literature data shows that the material synthesized by the modified-Pechini method has a larger specific surface area in relation to other methods [12,13,40]. The support had a surface area of 5.3 m^2 g^{-1}, while the SrSnO$_3$@ZrO$_2$ system presented a specific surface area of 8.1 m^2 g^{-1}. In spite of the small amount of SrSnO$_3$ on the SrSnO$_3$@ZrO$_2$ system (7%), a higher surface area was observed after deposition as a consequence of a better dispersion of SrSnO$_3$ as indicated by the TEM image. This better dispersion leads to more accessible catalytic sites and is expected to improve the catalytic activity.

Zeta potential measurements are displayed in Figure 3. A small increase in the point of zero charge (PZC) from 4.5 to 5.0 was observed when SrSnO$_3$ was deposited on ZrO$_2$ and may be indicative of the polarizing influence of the support due to a strong metal support interaction (SMSI). that SrSnO$_3$ largely defines the surface properties of the SrSnO$_3$@ZrO$_2$ composite, indicating a high level of surface coverage.

Figure 3

XPS measurements were carried out to determine the chemical composition and the oxidation states of the elements on the surface of the SrSnO$_3$ and SrSnO$_3$@ZrO$_2$ materials, besides evaluating the interaction between the active SrSnO$_3$ catalyst and the supporting ZrO$_2$ phase. XPS survey spectra (Figure 4a) confirm that Sr, Sn, and O elements are present in SrSnO$_3$ and SrSnO$_3$@ZrO$_2$ samples. The presence of the C signal in XPS spectra is from the SrCO$_3$ secondary phase in the samples as previously evidenced by XRD (Figure 1), and IR and Raman results (SD Figures S1 and S2). An important issue regarding the formation of the SrSnO$_3$@ZrO$_2$ material is the non-homogeneity and

9

dispersion of the SrSnO$_3$ shell layer covering the ZrO$_2$ inner material as suggested by TEM. Because of this morphological characteristic of the SrSnO$_3$@ZrO$_2$ sample and due to the penetration depth of the X-ray beam, a signal corresponding to the Zr element typical of ZrO$_2$ due to the support is observed in the spectrum with a smaller intensity compared to the other cations, in spite of the greater amount of ZrO$_2$ (93 mass%).

Figure 4

The detailed photoelectron Sr 3d, Sn 3d, O 1s and Zr 3d scans of the samples are shown in Figure 4b-e. For comparison, the XPS peaks of Sr 3d, Sn 3d and O 1s pertaining to SrSnO$_3$ and SrSnO$_3$@ZrO$_2$ materials are grouped together in Figure 4b-d, while the Zr 3d scan is shown by itself in Figure 4e. All the Sr 3d, Sn 3d and O 1s spectra clearly show a broadening of the peaks and a decrease in their intensity after depositing the SrSnO$_3$ phase on ZrO$_2$, which reflects an interfacial electronic interaction between the catalyst and the support. Moreover, peak shifts to lower binding energies observed in the Sn 3d (Figure 4c) and O1s (Figure 4d) spectra of SrSnO$_3$@ZrO$_2$ in comparison to SrSnO$_3$ further suggest the formation of the core-shell-like system.

It is also worth mentioning that the intensity of Sr 3d and Zr 3d peaks are lower than that of Sn 3d (Figure 4c) and O 1s (Figure 4d) and this might be attributed to the Sr-O-Zr bonding interaction created at the interface of the materials, which may impact the band gap structure. The pronounced change in the intensity and peak shape in the Sr 3d XPS spectra (Figure 4b) is noticed, besides the increase of the spin-orbit coupling energy Sr 3$d_{3/2}$ and 3$d_{5/3}$ from $\Delta E = 1.55$ eV (in SrSnO$_3$) to $\Delta E = 1.65$ eV (in SrSnO$_3$@ZrO$_2$) close to the values reported by Alammar $et\ al.$[41]. The increase in the spin-orbit energy after SrSnO$_3$ deposition indicates a perturbation in the local environment around the Sr and reinforces the suggestion of a Sr-O-Zr interface composition in SrSnO$_3$@ZrO$_2$. In addition to that, the Zr 3d XPS (Figure 4e) shows that the Zr 3d core level splits into Zr3$d_{5/3}$ and Zr3$d_{3/2}$ levels and the estimated spin-orbit splitting of $\Delta E = 2.32$ eV reveals that the valence state of Zr is 4+ at the

10

interface of SrSnO$_3$@ZrO$_2$ sample [42,43]. The high intensity of Sn $3d$ (Figure 4c) and O $1s$ (Figure 4d) peaks in the XPS spectra indicates that Sn-O environments are prominent at the surface of both materials as expected and in good accordance with [13,41]. The Sn $3d$ XPS spectra can be fitted into four peaks (two corresponding to Sn $3d_{3/2}$ and other two to Sn $3d_{5/2}$ levels) located at different binding energies as indicated in Figure 4c. This fourfold fitting reveals the existence of mixed Sn valences (Sn^{4+} and Sn^{2+}) present on the surface of the materials, in accordance with Aragon *et al.* [44], with a higher amount of Sn^{2+} on the surface of SrSnO$_3$@ZrO$_2$, indicated by the higher intensity of the Sn^{2+} band after deconvolution. The O $1s$ spectra (Figure 4d) can be deconvoluted into three peaks. The highest intense peak located at 530.3-530.7 eV and the one located at 528.7-529.9 eV are due to structural oxygen (O^{stru}) associated with the chemical states Sn^{2+} and Sn^{4+} in the perovskite surface, respectively. This assignment is confirmed by other authors [11,44] who associated the O peak 529 eV to an unreduced lattice region while the O peak at 530-531 eV was assigned to an oxygen deficient region. Li et al [15] associated the third peak located at 531.3-532.2 eV with the hydroxyl group. This protonated surface may be formed to stabilize the reduced Sn(II) state, as observed in the Sn 3d XPS spectra, giving rise to a n-type semiconductor.

The UV-vis spectra and the corresponding optical band gap values of SrSnO$_3$, ZrO$_2$ and SrSnO$_3$@ZrO$_2$ samples calcined at 1073 K are inferred in Figure 5. According to Moshtaghi *et al.* [23], SrSnO$_3$ exhibits a higher energy absorption region at around 300 nm, which is assigned to the transition from the O $2p$ orbital to the Sn $5s$ orbital [11,24]. Considering a direct band gap transition [15] (Figure 5), the experimental value estimated for SrSnO$_3$ was $E_g = 4.0$ eV, in agreement to the reported data [27,45], whereas the experimental direct E_g value of ZrO$_2$ was 5.0 eV, in agreement with the data reported by Aflaki *et al.*[46], indicating that ZrO$_2$ is an insulating material. The SrSnO$_3$@ZrO$_2$ system presented show a main transition at 4.3 eV with smaller contributions at 3.6 and 4.6 eV. It is likely that the spectrum reflects the influence of the two different materials – SrSnO$_3$ and ZrO$_2$ on each other, so the band gap of 4.3 eV may be assigned to SrSnO$_3$. In general, the optical band gap is influenced by the presence of structural and/or electronic defects in the lattice and the

11

change in the values in comparison to the pure materials may be due to the interaction between the two materials and to the Sn(IV) reduction to Sn(II) associated to oxygen vacancies, as indicated by XPS results.

Figure 5

UV-vis absorption data indicate the allowed electronic transitions in the semiconductor but do not reveal the energy (potential) positions of the relevant electronic states. These are fundamental to the viability of the redox (charge transfer) processes that can occur at the photocatalyst surface. If carrier concentrations (N_D) are sufficiently high, the conduction band edge position (E_{CB}) is equivalent to the flat band potential, which can be determined by electrochemical impedance spectroscopy (EIS) measurements (see Figure 6). An equivalent (Randles) circuit (inset of Figure 6a), has been used to model the data, enabling the Mott-Schottky approach and application of Equation (1); details are provided in the Supplementary data [47,48].

$$C^{-2} = \frac{2}{\varepsilon \varepsilon_0 A^2 e N_D}\left(V - V_{fb} - \frac{kT}{e}\right) \qquad (1)$$

Where: C is the capacitance, V the applied potential, V_{fb} the flat band potential, k the Boltzmann constant, T the temperature, ε the dielectric constant (considered as 12 in the present work [49,50]), ε_0 the vacuum permittivity, A the area of the working electrode, e the electronic charge and N_D the number of donors. E_{CB}, together with the band gap information, allows the valence band edge position (E_{VB}), can then be calculated; $E_{CB} - E_G = E_{VB}$.

Figure 6

12

Several authors have applied Mott Schottky analyses in evaluation of different materials, including composites, to determine the flat band potential as well as the number of donors. For instance, Amer et al. [51] evaluated the influence of the ZrN layers synthesized by atomic layer deposition on the properties of ZrO_2 nanotubes. According to the authors, V_{fb} values of the bare nanotube and of the ZrN/ZrO_2 core/shell sample were obtained with good accuracy and the band gap structures of both samples were proposed. Chen et al. [52] determined the V_{fb} and N_D values of mixed oxide films (ZrO_2, TiO_2, $ZrTiO_4$ and Nb_2O_5) formed by microarc oxidation on the surface of Ti-39Nb-5Zr alloys, and Shinde et al.[53] characterized Fe_2O_3 thin films deposited on FTO substrates with and without ZrO_2 underlayer.

EIS and band gap data are summarized in Figure 6. Mott Schottky analyses (Figure 6a) identifies almost the same flat band potentials (V_{fb}) for $SrSnO_3$ and $SrSnO_3@ZrO_2$; -0.27 and -0.26 V vs NHE respectively, which are close to the value reported by Li et al. [15] for $SrSnO_3$. Moreover, Ismael et al. [54] determined the V_{fb} value for the same commercial ZrO_2 used in the present work by Mott Schottky analysis and obtained V_{fb} = -0.75 V vs NHE, which is much more negative than the perovskite one and confirms that the experimental value obtained for the composite in the present work is due to the $SrSnO_3$ perovskite. It is also important to consider that $SrSnO_3@ZrO_2$ may have nanoparticulate $SrSnO_3$ capable of behaving electrochemically as isolated $SrSnO_3$ would but being better dispersed. $SrSnO_3$ at the $SrSnO_3$-ZrO_2 interface is likely to have different behaviour due to heterojunction effects, but the overall effect will be related to the volumetric distribution of the two environments.

Application of the band gap data (E_G) extrapolated from Figure 5 permits the construction of a band structure model (Figure 6b). According to XPS, both Sn(IV) and Sn(II) are present on the $SrSnO_3$ and $SrSnO_3@ZrO_2$ surfaces. Sn(II) electrons, with lower binding energies, are likely to occupy inter-band states below the conduction band (Sn (IV)), which if sufficiently populated, would account for lower energy transitions in the UV-vis spectra.

13

The value of N_D was calculated from the slope of the Mott-Schottky plot and values of 1.4 x 10^{20} cm^{-3} and 2.1 x 10^{20} cm^{-3} were obtained for $SrSnO_3$ and $SrSnO_3@ZrO_2$ samples. These values are smaller than those reported by Hadjarab *et al.* [55] for $SrSnO_3$:La (1.04 x 10^{21} cm^{-3}) and for $BaSnO_3$-$_\delta$ (3.07 x 10^{21} cm^{-3}) [56], probably due to their doping or reduction processes, which increase the number of donors. For undoped materials, literature reports very low electrical conductivities of about 1.0 x 10^{-7} S m^{-1} or lower [57,58], while a higher conductivity is reported for reduced materials (σ = 0.33 S m^{-1}). According to Wang *et al.*[59], such conductivity would be attained by a carrier concentration of about 3 x 10^{19} cm^{-3}. In the present case, the high N_D values indicate that reduced states are likely to be present in the $SrSnO_3$, in agreement to the XPS measurements (Figure 4c) and UV-vis spectra (Figure 5), which showed the presence of Sn(II) on the surface and gives rise to n-type semiconductor properties.

3.2. Photocatalytic tests

UV-Vis spectra of the RNL solution after photocatalytic tests are showed in the Figure 7. Photolysis tests indicated that the energy of the lamp was not able to degrade the dye. High photocatalytic efficiency was attained using $SrSnO_3$ as catalyst, with 90% of the dye solution decolorization after 10 h. The kinetics are favourable at the beginning of the reaction, with 18% of decolorization after 60 min under UV irradiation, at pH 6 (Figure S.4b of the supplementary data). Similar activities were observed for solutions with pH 3.5 and 6 up to 2 h of reaction, decreasing after this period for solutions with pH 3.5, for which 83% of decolorization is reached after 10 h (Figure S.4.a).

Data previously reported indicate that the high photocatalytic activity of the orthorhombic $SrSnO_3$ is due to the distorted SnO_6 octahedral lattice [11,25]. According to literature, these octahedra are connected by corner sharing that promote the charge carrier movement and therefore hence charge transfer reactions on the catalyst surface [10,21].

14

Figure 7

The $SrSnO_3@ZrO_2$ system also exhibits high photocatalytic activity at pH = 6, with a linear performance up to 2 h reaching 63% of decolorization, and 98% after 10 h. It is important to highlight that such efficiency is due to the $SrSnO_3$ active phase in spite of its smaller amount on the $SrSnO_3@ZrO_2$ system (only 7 mass% of $SrSnO_3$), as the photocatalytic activity of ZrO_2 was low, reaching only 40% of discoloration after 10 h. Comparing $SrSnO_3@ZrO_2$ and $SrSnO_3$ the decolorization was almost twice for the supported catalyst after 60 min and 120 min with a higher reaction rate, while a smaller difference was observed for longer reaction periods. This behavior may be assigned to the better dispersion of $SrSnO_3$ on the ZrO_2 surface, which increases the availability of active sites for photocatalytic reaction. Both $SrSnO_3$ and $SrSnO_3@ZrO_2$ presented a lower rate of activity in solutions at pH 3.5 than at pH = 6.

A better understanding of the data concerning discoloration can be achieved by the kinetic analysis, which was performed considering pseudo first-order kinetics, as displayed in the inset of Figure 7. The detailed results of the linear fit are presented in Table S.1 of the Supplementary data. Rate constant values of 0.182 h^{-1}, 0.0481 h^{-1} and 0.208 h^{-1} were obtained for $SrSnO_3$, ZrO_2 and $SrSnO_3@ZrO_2$, respectively, at pH 3.5, while values of 0.232 h^{-1}, 0.0424 h^{-1} and 0.359 h^{-1} were obtained for $SrSnO_3$, ZrO_2 and $SrSnO_3@ZrO_2$, respectively, at pH 6. These data confirm the improvement of the catalytic activity after deposition of $SrSnO_3$ on ZrO_2 and highest activity at pH 6. At this pH, the rate constant of $SrSnO_3@ZrO_2$ is 1.5 times higher than that of $SrSnO_3$ and 8.5 times higher than that of ZrO_2. Considering that only 7% of $SrSnO_3$ was deposited on ZrO_2, this remarkable improvement may be assigned to the interfacial coupling between $SrSnO_3$ and ZrO_2, as previously stated. Moreover, comparison with the previous publication of our research group [32], indicates that the lowest crystallinity of $SrSnO_3$ after deposition does not seem to be responsible for its highest activity. In this previous paper, $SrSnO_3$ was calcined at a lower temperature and a higher short-range

disorder was attained as indicated by the broad bands in the infrared spectrum and in the Raman spectrum and also by the smallest band gap value. Despite this, the discoloration percentages of both materials are very similar. Comparison of the photocatalytic activity with P25 was also performed, as displayed in Figure S.5 of the Supporting data. A rate constant value of 3.01 h^{-1} was obtained, which confirms the highest activity of this material.

Comparison of the photocatalytic data with UV-vis spectra and XPS measurements brings interesting points. The UV-vis spectrum (Figure 5) of $SrSnO_3@ZrO_2$ suggests a smaller carrier concentration than unsupported $SrSnO_3$, which may be assigned to the small amount of $SrSnO_3$ (7 mass %) in the $SrSnO_3@ZrO_2$. On the other hand, XPS data indicate a bigger amount of Sn(II) on the $SrSnO_3@ZrO_2$ surface (Figure 4c), which is likely to enhance the photocatalytic activity due to a reduced carrier recombination, and increased electronic conductivity, as already observed for other perovskites [60].

Chen et al. [61] and Huang et al. [62] have studied the influence of spontaneous polarization in non-centrosymmetric materials with piezoelectric properties on the recombination of photogenerated electrons and holes during photocatalytic process. Increase in the distortion of the polyhedron by ionic replacement or by oxygen vacancies promotes bulk charge separation and favors surface reactions. The presence of oxygen vacancies also improves the migration of photogenerated electrons and holes to the surface and their rapid transfer to the catalytic sites [61]. Recently, our research group [63] showed that Eu doping into $SrSnO_3$ lattice increased short- and long-range order, induced a distortion in the SnO_6 and created Eu midgap states. All these factors apparently favored charge separation and improved the photocatalytic activity. This way, besides the better dispersion upon deposition, the highest amount of reduced Sn(II) may also improve the photocatalytic activity.

Based on UV-vis spectra, it was also possible to estimate the dye degradation, since the UV-vis bands assigned to the aminoacetanilide group of the dye molecule were also affected by the photocatalytic process, as shown in Figure 7. After 10 h under irradiation at pH = 6, $SrSnO_3$ was able to reduce the intensities of all the absorption bands of the dye solution, namely the band related to the

16

chromophore group (λ = 411 nm) and those ones assigned to the aromatic group (maximum absorbances at 292 and 238 nm) reaching approximately 65% and 75% of band reduction, respectively. For the SrSnO$_3$@ZrO$_2$ catalyst, this reduction reached 45% for the band with maximum at 238 nm and 65% for the one at 292 nm.
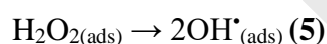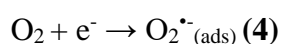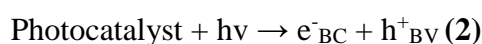
Although a higher efficiency is observed for P25 concerning the discoloration, a meaningful increase in the absorption below 325 nm is also observed and indicates that other compounds are formed during photodegradation process. This increase was not observed when SrSnO$_3$-containing systems were used as photocatalysts, as displayed in Figure 7.

According to the zeta potential (Figure 3) measurements, the photocatalysts present a positive surface at pH 3.5 and a negative surface at the pH 6. RNL has a negative charge for both solutions, as pKa$_1$ = 3, pKa$_2$ = 3.5, pKa$_3$ = 6, but with a greater negative charge at pH = 6. As a consequence, different behaviors are observed at pH 3.5 or 6: at pH 3.5, adsorption is favored by the opposite charges of the surface and dye and adsorption values of 16%, 18% and 13% after 10 h in the dark are obtained for SrSnO$_3$, SrSnO$_3$@ZrO$_2$ and ZrO$_2$, respectively. Repulsion between surface and dye at pH = 6 decreases the azo-dye adsorption on the material surface, which was smaller, with adsorption values of 10%, 7% and 4% after 10 h in the dark for SrSnO$_3$, SrSnO$_3$@ZrO$_2$ and ZrO$_2$, respectively. Despite this, adsorption cannot be ruled out, as surface may be modified during irradiation and adsorption may still occur. This behavior was also indicated by the adsorption curves (Figure S.6 of the Supplementary data), which show a gradual increase in the amount of adsorbed dye onto the surfaces of all materials during 10 h of test in the dark. Moreover, zeta potential values are smaller than 20 mV, which is relatively weak and does not condition a strong repulsion.

A better understanding of the photocatalytic process was attained using probes for •OH radicals and scavengers for •OH radicals, electrons and holes, as described below.

3.3. Pathway for the photocatalytic degradation

17

According to literature [4,64], during photocatalysis the photogenerated electrons can interact with acceptor molecules, such as O_2, adsorbed on the surface of the semiconductor or dissolved in water, leading to the formation of a superoxide, and subsequently to $^\bullet OH$ radicals. On the other hand, photogenerated holes can oxidize species such as OH^- or H_2O, which decompose into free $^\bullet OH$ radicals. Different reactive oxygen species may be formed during the process, which are responsible for the oxidation of the organic molecule and the production of intermediates, generating CO_2 and H_2O. The reactions are represented in Equations (2) to (6) [4].

$$\text{Photocatalyst} + hv \rightarrow e^-_{BC} + h^+_{BV} \ (2)$$

$$H_2O_{(ads)} + h^+ \rightarrow {}^\bullet OH_{(ads)} + H^+_{(ads)} \ (3)$$

$$O_2 + e^- \rightarrow O_2^{\bullet-}{}_{(ads)} \ (4)$$

$$H_2O_{2(ads)} \rightarrow 2OH^\bullet{}_{(ads)} \ (5)$$

$${}^\bullet OH + \text{dye} \rightarrow \text{intermediates} \rightarrow CO_2 + H_2O \ (6)$$

Evaluation of the formation of hydroxyl radical was done by the photooxidation of terephthalic acid in accordance to the procedure described by Teixeira *et al.* [32]. After photocatalytic tests, both materials showed a meaningful increase in the intensity of the luminescent band at 420 nm, as displayed in Figure 8. According to this result a high amount of hydroxyl radicals is formed during irradiation of the TA solution in the presence of both catalysts, and a higher intensity was attained for $SrSnO_3@ZrO_2$. These radicals may be formed by H_2O oxidation in agreement to Eq. (4) or by O_2 reduction according to Eq. (5) to (8).

Figure 8

This result was confirmed with the use of isopropanol, a well-known scavenger for hydroxyl radicals (Zhu *et al.*[65]), which inhibited the photocatalytic process at pH 3 and 6, as observed in

the Figure 9. After its addition, only 20% and 24% of decolorization was reached after 10 h of irradiation using $SrSnO_3$ and $SrSnO_3@ZrO_2$, respectively.
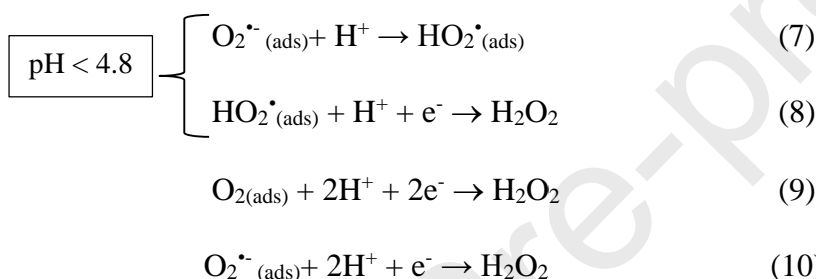
Figure 9

EDTA was employed as a hole scavenger and confirmed the influence of H_2O oxidation on the formation of hydroxyl radicals. Comparison of the EDTA oxidation potential with the valence band edge indicates that electron transfer is feasible, as displayed in Figure 6b. Moreover, electron transfer from H_2O/OH^- to the valence band of the semiconductors is also feasible for both samples. According to the results displayed in Figure 9, a meaningful decrease in the decolorization was observed, with a higher decrease for $SrSnO_3@ZrO_2$. This effect is more meaningful at pH 3.5 for both catalysts. According to Zhu *et al.* [65], besides suppression of holes, EDTA also decreases the photocatalytic activity due to a competitive adsorption on the material surface. EDTA has a negative charge at pH 3.5 and 6 (pK_a = 2.0, 2.7, 6.2 and 10.3), while both photocatalysts have a positive surface charge at pH 3.5 and a negative surface charge at pH 6, as indicated by zeta potential measurements (Figure 3). As a consequence, a bigger adsorption may occur at pH 3.5, leading to the smaller decolorization of the solution. The importance of the holes in the photocatalytic activity of $SrSnO_3$ was also observed using formic acid as hole scavenger, as recently reported by our research group [32].

The role of electrons on the photodegradation of RNL dye was evaluated using Ag^+ as electron scavenger (Figure 9). According to the energy diagram (Figure 6b), electron transfer from the semiconductor conduction band to Ag^+ is energetically feasible, for both photocatalysts, whatever the pH of the solution. At pH 3.5, a meaningful increase in the decolorization percentage was observed after Ag^+ addition into the solution. The increase of the photocatalytic activity may be assigned to the deposition of Ag on the catalyst surface after Ag^+ reduction, improving the electron capture by O_2, as already reported by Junploy *et al.* [66]. At the end of the photocatalytic test, stabilization of the

decolorization occurs, which may be related to the formation of metallic silver in suspension that avoids light absorption by the catalyst affecting its efficiency [67]. In spite of the highest activity after Ag^+ addition for almost all of the photocatalytic tests, a meaningful difference is observed between the profile of the curves at pH 3.5 and pH 6 (Figure 9), as a smaller difference of decolorization with and without Ag^+ was observed at pH 6, especially when $SrSnO_3@ZrO_2$ was used as photocatalyst.

Reactions involving the reduction of adsorbed oxygen are described in equations (7) and (8) for pH up to 4.8, in which E^o varies according to the Nernst equation. Other, multi-electron transfer reactions are possible at higher potentials, i.e. as in equations (9) and (10).

$$\boxed{pH < 4.8} \begin{cases} O_2^{\bullet-}{}_{(ads)} + H^+ \rightarrow HO_2^{\bullet}{}_{(ads)} & (7) \\ HO_2^{\bullet}{}_{(ads)} + H^+ + e^- \rightarrow H_2O_2 & (8) \end{cases}$$

$$O_{2(ads)} + 2H^+ + 2e^- \rightarrow H_2O_2 \qquad (9)$$

$$O_2^{\bullet-}{}_{(ads)} + 2H^+ + e^- \rightarrow H_2O_2 \qquad (10)$$

At pH 3.5, formation of $HO_2^{\bullet}$ (reaction (7)) is feasible as E^o for $O_2, H^+/\bullet O_2H$ is more positive than the conduction band edge of the catalyst. However, by pH 6, E_{CB} of both $SrSnO_3$ and $SrSnO_3@ZrO_2$ has reduced to below the value of E^o for the $O_2/\bullet O_2^-$ couple, which is constant for pH > 4.8 at -0.33 V, providing $O_2^{\bullet-}$ as a viable reduction product and sink for photogenerated electrons.

This difference is likely to account for the observed difference in photocatalytic behaviour at the different pHs. According to the literature, defects such as oxygen vacancies are active sites for the electron transfer to adsorbed O_2 molecules and improve photocatalytic reactions [68]. In their photocatalytic study of $MSnO_3$ (M = Ca, Sr, Ba) perovskites, Li *et al.* [15] showed that when no oxygen vacancies are present, almost no O_2^- was produced by $CaSnO_3$, as indicated by ESR using DMPO as spin trapping agent for O_2^-, whereas electron transfer to absorbed O_2 is clearly observed when oxygen vacancies are created in the solid.

4. Conclusions

The results of this study showed that $SrSnO_3$ and $SrSnO_3@ZrO_2$ photocatalysts were efficient in the photodegradation of the Remazol RNL dye under UV light and $SrSnO_3@ZrO_2$ system was more efficient when compared to unsupported $SrSnO_3$. No meaningful change in the band edge positions (VB and CB) of $SrSnO_3$ was noticed after its deposition on ZrO_2 support, and the greater efficiency of $SrSnO_3@ZrO_2$ was related to its reduced surface character as indicated by XPS results and to a better dispersion of $SrSnO_3$ on the ZrO_2 surface, enhancing a higher activity even with a smaller amount of active phase ($SrSnO_3$). The formation of hydroxyl radicals was confirmed using terephthalic acid as a probe and the use of the hydroxyl radical scavenger promoted inhibition around 76%, indicating that this radical is mainly responsible for the photocatalytic process. It was also confirmed that holes have an important role in the photocatalytic process, which is consistent with the observed band structure. Photocatalytic activity also depends on the pH of the solution, due to the different reactive oxygen species, with a greater efficiency at pH 6, probably due the most efficient electron transfer from conduction band to O_2.

References

[1]   L. V. Bora, R.K. Mewada, Visible/solar light active photocatalysts for organic effluent treatment: Fundamentals, mechanisms and parametric review, Renew. Sustain. Energy Rev. 76 (2017) 1393–1421.

[2]   S. Song, L. Xu, Z. He, H. Ying, J. Chen, X. Xiao, B. Yan, Photocatalytic degradation of C.I. Direct Red 23 in aqueous solutions under UV irradiation using $SrTiO_3/CeO_2$ composite as the catalyst, J. Hazard. Mater. 152 (2008) 1301–1308.

[3]   C.G. Silva, W. Wang, J.L. Faria, Photocatalytic and photochemical degradation of mono-, di- and tri-azo dyes in aqueous solution under UV irradiation, J. Photochem. Photobiol. A Chem. 181 (2006) 314–324.

[4]   M.A. Rauf, M.A. Meetani, S. Hisaindee, An overview on the photocatalytic degradation of azo dyes in the presence of TiO_2 doped with selective transition metals, Desalination. 276 (2011) 13–27.

[5]   E. Brillas, C.A. Martínez-Huitle, Applied Catalysis B : Environmental Decontamination of wastewaters containing synthetic organic dyes by electrochemical methods . An updated review, Applied Catal. B, Environ. 166–167 (2015) 603–643.

[6]   M. Ghiasi, A. Malekzadeh, Solar photocatalytic degradation of methyl orange over $La_{0.7}Sr_{0.3}MnO_3$ nano-perovskite, Sep. Purif. Technol. 134 (2014) 12–19.

[7]   X. Hu, Y. Tang, T. Xiao, J. Jiang, Z. Jia, D. Li, B. Li, L. Luo, Rapid Synthesis of Single-Crystalline $SrSn(OH)_6$ Nanowires and the Performance of $SrSnO_3$ Nanorods Used as Anode Materials for Li-Ion Battery, J. Phys. Chem. C. 114 (2010) 947–952.

[8]   Y. Shimizu, M. Shimabukuro, H. Arai, T. Seiyama, Humidity-Sensitive Characteristics of La^{3+}-Doped and Undoped $SrSnO_3$, J. Electrochem. Soc. 136 (1989) 1206.

[9]   Y. Li, H. Zhang, B. Guo, M. Wei, Enhanced efficiency dye-sensitized $SrSnO_3$ solar cells prepared using chemical bath deposition, Electrochim. Acta. 70 (2012) 313–317.

[10] W.F. Zhang, J. Tang, J. Ye, Photoluminescence and photocatalytic properties of $SrSnO_3$ perovskite, Chem. Phys. Lett. 418 (2006) 174–178.

[11] C.W. Lee, D.W. Kim, I.S. Cho, S. Park, S.S. Shin, S.W. Seo, K.S. Hong, Simple synthesis and characterization of $SrSnO_3$ nanoparticles with enhanced photocatalytic activity, Int. J. Hydrogen Energy. 37 (2012) 10557–10563.

[12] W. Wang, S. Liang, K. Ding, J. Bi, J.C. Yu, P.K. Wong, L. Wu, Microwave hydrothermal synthesis of $MSnO_3$ (M^{2+} = Ca^{2+}, Sr^{2+}, Ba^{2+}): effect of M^{2+} on crystal structure and photocatalytic properties, J. Mater. Sci. 49 (2014) 1893–1902.

[13] F. Zhong, H. Zhuang, Q. Gu, J. Long, Structural evolution of alkaline earth metal stannates

22

MSnO$_3$ (M = Ca, Sr, and Ba) photocatalysts for hydrogen production, RSC Adv. 6 (2016) 42474–42481.

[14] C. Gómez-Solís, J. Oliva, L.A. Diaz-Torres, J. Bernal-Alvarado, V. Reyes-Zamudio, A. Abidov, L.M. Torres-Martinez, Efficient photocatalytic activity of MSnO$_3$ (M: Ca, Ba, Sr) stannates for photoreduction of 4-nitrophenol and hydrogen production under UV light irradiation, J. Photochem. Photobiol. A Chem. 371 (2019) 365–373.

[15] H. Li, Y. Gao, D. Gao, Y. Wang, Effect of oxide defect on photocatalytic properties of MSnO$_3$ (M = Ca, Sr, and Ba) photocatalysts, Appl. Catal. B Environ. 243 (2019) 428–437.

[16] T. Schumann, S. Raghavan, K. Ahadi, H. Kim, S. Stemmer, Structure and optical band gaps of (Ba,Sr)SnO$_3$ films grown by molecular beam epitaxy, J. Vac. Sci. Technol. A. 34 (2016) 050601.

[17] Q. Liu, J. Dai, X. Zhang, G. Zhu, Z. Liu, G. Ding, Perovskite-type transparent and conductive oxide films: Sb- and Nd-doped SrSnO$_3$, Thin Solid Films. 519 (2011) 6059–6063.

[18] H. Mizoguchi, H.W. Eng, P.M. Woodward, Probing the Electronic Structures of Ternary Perovskite and Pyrochlore Oxides Containing Sn^{4+} or Sb^{5+}, Inorg. Chem. 43 (2004) 1667–1680.

[19] A.K. Prodjosantoso, Q. Zhou, B.J. Kennedy, Synchrotron X-ray diffraction study of the Ba$_{1-x}$SrSnO$_3$ solid solid solution, J. Solid State Chem. 200 (2013) 241–245.

[20] H. Chen, N. Umezawa, Sensitization of perovskite strontium stannate SrSnO$_3$ towards visible-light absorption by doping, Int. J. Photoenergy. 2014 (2014) 3–6.

[21] W. Zhang, J. Tang, J. Ye, Structural, photocatalytic, and photophysical properties of perovskite MSnO$_3$ (M = Ca, Sr, and Ba) photocatalysts, J. Mater. Res. 22 (2007) 1859–1871.

[22] T. Alammar, I.I. Slowing, J. Anderegg, A.V. Mudring, Ionic-Liquid-Assisted Microwave Synthesis of Solid Solutions of Sr$_{1-x}$Ba$_x$SnO$_3$ Perovskite for Photocatalytic Applications, ChemSusChem. (2017) 3387–3401.

[23] S. Moshtaghi, S. Gholamrezaei, M. Salavati Niasari, P. Mehdizadeh, New controllable procedure for preparation of SrSnO$_3$ nanostructures: photo-degradation of azo dyes and photovoltaic measurement, J. Mater. Sci. Mater. Electron. 27 (2016) 414–424.

[24] P. Junploy, S. Thongtem, T. Thongtem, Photoabsorption and photocatalysis of SrSnO$_3$ produced by a cyclic microwave radiation, Superlattices Microstruct. 57 (2013) 1–10.

[25] W. Wang, J. Bi, L. Wu, Z. Li, X. Fu, Hydrothermal synthesis and catalytic performances of a new photocatalyst CaSnO$_3$ with microcube morphology, Scr. Mater. 60 (2009) 186–189.

[26] S. Moshtaghi, S. Zinatloo-Ajabshir, M. Salavati-Niasari, Preparation and characterization of BaSnO$_3$ nanostructures via a new simple surfactant-free route, J. Mater. Sci. Mater. Electron.

27 (2016) 425–435.

[27] G.L. Lucena, J.J.N. Souza, A.S. Maia, L.E.B. Soledade, E. Longo, A.G. Souza, I.M.G. Santos, New methodology for a faster synthesis of $SrSnO_3$ by the modified Pechini method, Cerâmica. 59 (2013) 249–253.

[28] D.L. Wood, J. Tauc, Weak Absorption Tails in Amorphous Semiconductors, Phys. Rev. B. 5 (1972) 3144–3151.

[29] A. Folli, J.Z. Bloh, E.-P. Beukes, R.F. Howe, D.E. Macphee, Photogenerated Charge Carriers and Paramagnetic Species in (W,N)-Codoped TiO_2 Photocatalysts under Visible-Light Irradiation: An EPR Study, J. Phys. Chem. C. 117 (2013) 22149–22155.

[30] S. Chaiwichian, K. Wetchakun, W. Kangwansupamonkon, N. Wetchakun, Novel visible-light-driven $BiFeO_3$-Bi_2WO_6 nanocomposites toward degradation of dyes, J. Photochem. Photobiol. A Chem. 349 (2017) 183–192.

[31] K. Ishibashi, A. Fujishima, T. Watanabe, K. Hashimoto, Quantum yields of active oxidative species formed on TiO_2 photocatalyst, J. Photochem. Photobiol. A Chem. 134 (2000) 139–142.

[32] A.R.F.A. Teixeira, A. de Meireles Neris, E. Longo, J.R. de Carvalho Filho, A. Hakki, D. Macphee, I.M.G. dos Santos, $SrSnO_3$ perovskite obtained by the modified Pechini method—Insights about its photocatalytic activity, J. Photochem. Photobiol. A Chem. 369 (2019) 181–188.

[33] K.F. Moura, L. Chantelle, D. Rosendo, E. Longo, I.M.G. dos Santos, Effect of Fe^{3+} Doping in the Photocatalytic Properties of $BaSnO_3$ Perovskite, Mater. Res. 20 (2017) 317–324.

[34] R. Palominos, J. Freer, M.A. Mondaca, H.D. Mansilla, Evidence for hole participation during the photocatalytic oxidation of the antibiotic flumequine, J. Photochem. Photobiol. A Chem. 193 (2008) 139–145.

[35] L.M. Pastrana-Martínez, S. Morales-Torres, V. Likodimos, J.L. Figueiredo, J.L. Faria, P. Falaras, A.M.T. Silva, Advanced nanostructured photocatalysts based on reduced graphene oxide-TiO_2 composites for degradation of diphenhydramine pharmaceutical and methyl orange dye, Appl. Catal. B Environ. 123–124 (2012) 241–256.

[36] X. Zhang, J. Hu, Y. Cao, J. Xie, W. Jia, S. Wang, D. Jia, Insights into Crystal Facets of Perovskite $SrSnO_3$ as High-Performance Photocatalysts toward Environmental Remediation, Chem. Eur. J. 24 (2018) 14111–14118.

[37] M.C.F. Alves, M.R. Nascimento, S.J.G. Lima, P.S. Pizani, J.W.M. Espinosa, E. Longo, L.E.B. Soledade, A.G. Souza, I.M.G. Santos, Influence of synthesis conditions on carbonate entrapment in perovskite $SrSnO_3$, Mater. Lett. 63 (2009) 118–120.

[38] J. Bohnemann, R. Libanori, M.L. Moreira, E. Longo, High-efficient microwave synthesis and characterisation of SrSnO$_3$, Chem. Eng. J. 155 (2009) 905–909.

[39] G. L. Lucena, A. da S. Maia, E. Longo, A. G. de Souza, I. M. G. dos Santos, A Facile Synthesis Method to Obtain SrSnO$_3$@AO$_2$ (A = Ti or Zr) Core Shell Systems, Curr. Phys. Chem. 5 (2016) 214–222.

[40] T.M. Lobo, R. Lebullenger, V. Bouquet, M. Guilloux-Viry, I.M.G. Santos, I.T. Weber, SrSnO$_3$:N – Nitridation and evaluation of photocatalytic activity, J. Alloys Compd. 649 (2015) 491–494.

[41] T. Alammar, I. Hamm, V. Grasmik, M. Wark, A.-V. Mudring, Microwave-Assisted Synthesis of Perovskite SrSnO$_3$ Nanocrystals in Ionic Liquids for Photocatalytic Applications, Inorg. Chem. 56 (2017) 6920–6932.

[42] Obaidullah. Md, T. Furusawa, I. Ahmed, N. Mohammed, M. Sato, N. Suzuki, A fast and facile microwave irradiation method for the synthesis of ZnO@ZrO$_2$ core-shell nanocomposites and the investigation of their optical properties, Adv. Powder Technol. 29 (2018) 1804–1811.

[43] J. Liu, M. Liao, M. Imura, A. Tanaka, H. Iwai, Y. Koide, Low on-resistance diamond field effect transistor with high-k ZrO$_2$ as dielectric, Scientific Reports 4 (2014) 6395.

[44] F.H. Aragón, I. Gonzalez, J.A.H. Coaquira, P. Hidalgo, H.F. Brito, J.D. Ardisson, W.A.A. Macedo, P.C. Morais, Structural and Surface Study of Praseodymium-Doped SnO2 Nanoparticles Prepared by the Polymeric Precursor Method, J. Phys. Chem. C. 119 (2015) 8711–8717.

[45] D.J. Singh, Q. Xu, K.P. Ong, X. Fan, Strain dependence of the optical properties and band gap of transparent conducting BaSnO$_3$ and SrSnO$_3$, Proc. SPIE - Thin Films for Solar and Energy Technology VI. 9177 (2014) 91770F.

[46] M. Aflaki, F. Davar, Synthesis, luminescence and photocatalyst properties of zirconia nanosheets by modified Pechini method, J. Mol. Liq. 221 (2016) 1071–1079.

[47] K. Gelderman, L. Lee, S.W. Donne, Flat-Band Potential of a Semiconductor: Using the Mott–Schottky Equation, J. Chem. Educ. 84 (2007) 685–685.

[48] J.Z. Bloh, A. Folli, D.E. Macphee, Adjusting Nitrogen Doping Level in Titanium Dioxide by Codoping with Tungsten: Properties and Band Structure of the Resulting Materials, J. Phys. Chem. C. 118 (2014) 21281–21292.

[49] M.K. Singh, J.W. Hong, N.K. Karan, H.M. Jang, R.S. Katiyar, S.A.T. Redfern, J.F. Scott, New cryogenic phase transitions in SrSnO$_3$, J. Phys. Condens. Matter. 22 (2010) 095901.

[50] W.W. Coffeen., Ceramic and Dielectric Properties of the Stannates, J. Am. Ceram. Soc. 36 (1953) 207–214.

[51]   A.W. Amer, M.A. El-Sayed, N.K. Allam, Tuning The Photoactivity of Zirconia Nanotubes-Based Photoanodes via Ultrathin Layers of ZrN: An Effective Approach toward Visible-Light Water Splitting, J. Phys. Chem. C. 120 (2016) 7025–7032.

[52]   L. Chen, Y. Qu, K. Wei, X. Jin, B. Liao, W. Xue, Fabrication and characterization of microarc oxidation films on Ti-39Nb-6Zr alloy at different voltages in KOH electrolyte, J. Alloys Compd. 725 (2017) 1158–1165.

[53]   P.S. Shinde, S.Y. Lee, S.H. Choi, H.H. Lee, J. Ryu, J.S. Jang, A Synergistic Effect of Surfactant and ZrO_2 Underlayer on Photocurrent Enhancement and Cathodic Shift of Nanoporous Fe_2O_3 Photoanode, Sci. Rep. 6 (2016) 32436.

[54]   M. Ismael, Y. Wu, M. Wark, Photocatalytic activity of ZrO_2 composites with graphitic carbon nitride for hydrogen production under visible light, New J. Chem. 43 (2019) 4455–4462.

[55]   B. Hadjarab, A. Bouguelia, M. Trari, Synthesis, physical and photo electrochemical characterization of La-doped $SrSnO_3$, J. Phys. Chem. Solids. 68 (2007) 1491–1499.

[56]   B. Hadjarab, M. Trari, M. Kebir, Physical characterization of the semiconducting deficient perovskite $BaSnO_{3-\delta}$, Mater. Sci. Semicond. Process. 29 (2015) 283–287.

[57]   V. Thangadurai, P. Schmid Beurmann, W. Weppner, Mixed oxide ion and electronic conductivity in perovskite-type $SrSnO_3$ by Fe substitution, Mater. Sci. Eng. B Solid-State Mater. Adv. Technol. 100 (2003) 18–22.

[58]   S. Singh, P. Singh, O. Parkash, D. Kumar, Synthesis, microstructure and electrical properties of Ti doped $SrSnO_3$, Adv. Appl. Ceram. 106 (2007) 231–234.

[59]   J. Wang, J. Huang, J. Meng, Q. Li, J. Yang, Double-hole codoped huge-gap semiconductor ZrO_2 for visible-light photocatalysis, Phys. Chem. Chem. Phys. 18 (2016) 17517–17524.

[60]   R. Hailili, C. Wang, E. Lichtfouse, Perovskite nanostructures assembled in molten salt based on halogen anions KX (X = F, Cl and Br): Regulated morphology and defect-mediated photocatalytic activity, Appl. Catal. B Environ. 232 (2018) 531–543.

[61]   F. Chen, Z. Ma, L. Ye, T. Ma, T. Zhang, Y. Zhang, H. Huang, Macroscopic Spontaneous Polarization and Surface Oxygen Vacancies Collaboratively Boosting CO_2 Photoreduction on $BiOIO_3$ Single Crystals, Adv. Mater. 32 (2020) 1908350.

[62]   H. Huang, S. Tu, C. Zeng, T. Zhang, A.H. Reshak, Y. Zhang, Macroscopic Polarization Enhancement Promoting Photo-and Piezoelectric-Induced Charge Separation and Molecular Oxygen Activation, Angew. Chemie - Int. Ed. 56 (2017) 11860–11864.

[63]   L. Chantelle, A.L. Menezes de Oliveira, B.J. Kennedy, J. Maul, M.R.S. da Silva, T.M. Duarte, A.R. Albuquerque, J.R. Sambrano, R. Landers, M. Siu-Li, E. Longo, I.M.G. dos Santos, Probing the Site-Selective Doping in $SrSnO_3$:Eu Oxides and Its Impact on the Crystal and

Electronic Structures Using Synchrotron Radiation and DFT Simulations, Inorg. Chem. 59 (2020) 7666-7680.

[64] A. Ajmal, I. Majeed, R.N. Malik, H. Idriss, M.A. Nadeem, Principles and mechanisms of photocatalytic dye degradation on TiO_2 based photocatalysts: A comparative overview, RSC Adv. 4 (2014) 37003–37026.

[65] X.D. Zhu, Y.J. Wang, R.J. Sun, D.M. Zhou, Photocatalytic degradation of tetracycline in aqueous solution by nanosized TiO_2, Chemosphere. 92 (2013) 925–932.

[66] P. Junploy, T. Thongtem, S. Thongtem, A. Phuruangrat, Decolorization of Methylene Blue by $Ag/SrSnO_3$ Composites under Ultraviolet Radiation, J. Nanomater. 2014 (2014) 1–10.

[67] Z. Ji, M.N. Ismail, D.M. Callahan, E. Pandowo, Z. Cai, T.L. Goodrich, K.S. Ziemer, J. Warzywoda, A. Sacco, The role of silver nanoparticles on silver modified titanosilicate ETS-10 in visible light photocatalysis, Appl. Catal. B Environ. 102 (2011) 323–333.

[68] N. Zhang, X. Li, H. Ye, S. Chen, H. Ju, D. Liu, Y. Lin, W. Ye, C. Wang, Q. Xu, J. Zhu, L. Song, J. Jiang, Y. Xiong, Oxide Defect Engineering Enables to Couple Solar Energy into Oxygen Activation, J. Am. Chem. Soc. 138 (2016) 8928–8935.

Figure captions

Fig. 1. X-ray diffraction patterns of the $SrSnO_3$ (a), ZrO_2 (b) and $SrSnO_3@ZrO_2$ (c) samples calcined at 1073 K. The peaks marked with (#), (*) and (°) in the patterns correspond to $SrSnO_3$, $SrCO_3$ and ZrO_2 phases, respectively.

Fig. 2. SEM (a), TEM (b) and EDX mapping (c) images of $SrSnO_3@ZrO_2$ sample.

Fig. 3. Zeta potential variation of $SrSnO_3$ (a), ZrO_2 (b) and $SrSnO_3@ZrO_2$ (c) as a function of the pH.

Fig. 4. (a) XPS survey spectra of $SrSnO_3$ and $SrSnO_3@ZrO_2$ samples and XPS deconvoluted scans of $SrSnO_3$ and $SrSnO_3@ZrO_2$ samples: (b) Sr 3d, (c) Sn 3d, (d) O 1s and (e) Zr 3d.

Fig. 5. UV-vis absorption spectra of $SrSnO_3$, ZrO_2 and $SrSnO_3@ZrO_2$ samples calcined at 1073 K, considering a direct band gap. The estimated band gap values (Eg) are indicated in the graph.

Fig. 6. (a) Evaluation of the V_{fb} of $SrSnO_3$ and $SrSnO_3@ZrO_2$ according to the Mott Schottky plot. (b) Energy level diagram, illustrating the band gap structure in agreement to the V_{fb} found in the present work. Standard potential of redox couples involved in the present work are presented for comparison in the right side. All values are observed at pH = 0, except for the $O_2/\bullet O_2^-$ one, which is obtained at pH > 4.8.

Fig. 7. UV-vis absorption spectra of the Remazol RNL dye, after photolysis and after irradiation during 10 h, in the presence of $SrSnO_3$ (a), ZrO_2 (b) or $SrSnO_3@ZrO_2$ (c). Insets show the kinetic plots of photo-degradation of the RNL at pH 3.5 (A) ad pH 6 (B).

Fig. 8. Fluorescence spectra of the TA solution after UVA irradiation in the presence of $SrSnO_3@ZrO_2$, after different periods of reaction. Inset: Intensity of the band at 420 nm after different periods of irradiation in the presence of $SrSnO_3$ or $SrSnO_3@ZrO_2$.

Fig. 9. Rate of RNL dye absorption in the presence of $SrSnO_3$ (a) and $SrSnO_3@ZrO_2$ (b), for dye solutions at pH 3.5 and pH 6, and using different scavengers: isopropanol (1.6 x 10^{-1} mol L^{-1}), $AgNO_3$ (5.0 x 10^{-4} mol L^{-1}) and EDTA (2.0 x 10^{-4} mol L^{-1}) as a function of the irradiation time.

Highlights

Title: Supporting the Photocatalysts on commercial oxide: An Effective Way to Enhance the

Photocatalytic Activity of $SrSnO_3$

- Azo-dye discolorization increased 1.8 times after deposition of $SrSnO_3$ on ZrO_2
- After deposition $SrSnO_3$ had higher amount of Sn(II) species and better dispersion
- Photocatalytic activity was correlated to the band gap structures determined by EIS
- Formation of •OH by H_2O reaction with holes was confirmed using scavengers

CRediT author statement

Title: Supporting the Photocatalysts on commercial oxide: An Effective Way to Enhance the Photocatalytic Activity of $SrSnO_3$

Authors:

Luzia Maria Castro Honorio: conceptualization, investigation, writing – original draft

André Menezes: formal analysis of the XPS data, writing – original draft

Edson Cavalcanti da Silva Filho: resources for XPS analysis

Josy Anteveli Osajima: resources for TEM analysis

Amer Hakki: investigation of the terephthalic acid photohydroxilation and of the Mott Schottky measurements

Donald E. Macphee: resources for the investigation of the terephthalic acid photohydroxilation and of the Mott Schottky measurements, writing – review & editing

Iêda Maria Garcia dos Santos: investigation of the terephthalic acid photohydroxilation and of the Mott Schottky measurements, writing – review & editing, supervision

$E_g = 3.6 - 4.3 - 4.6$ eV

$E_g = 5.0$ eV

$E_g = 4.0$ eV

SrSnO$_3$

SrSnO$_3$@ZrO$_2$

ZrO$_2$

$(\alpha h\nu)^2$

Energy (eV)

UV light

LUMO

e⁻ e⁻ e⁻ e⁻

h⁺ h⁺ h⁺ h⁺

HOMO

RNL

degradation products

O₂

$O_2^{\cdot-}$

e⁻

H_2O

·OH

RNL

de

h⁺

SrSnO₃@ZrO₂
Photocatalyst